Acta Crystallographica Section B
Structural Science
ISSN 0108-7681

Structural complexity of a polar perhydrotriphenylene inclusion compound brought to light by synchrotron radiation

Thomas Weber,[a]* Michael A. Estermann[a] and Hans-Beat Bürgi[b]

[a]Laboratory of Crystallography, Swiss Federal Institute of Technology Zürich, ETH Zentrum, Sonneggstrasse 5, CH-8092 Zürich, Switzerland, and [b]Laboratory of Chemical and Mineralogical Crystallography, University of Berne, Freiestrasse 3, CH-3012 Berne, Switzerland

Correspondence e-mail: weber@kristall.erdw.ethz.ch

Received 16 March 2001
Accepted 28 March 2001

The complex diffraction pattern of the heavily disordered co-crystals of perhydrotriphenylene and 1-(4-nitrophenyl)piperazine ($5C_{18}H_{30}\cdot C_{10}H_{13}N_3O_2$) has been investigated with synchrotron radiation and an area detector. Five (almost) complete, three-dimensional data sets have been obtained from the tips and the centre of a needle-like crystal at room temperature and 120 K. They revealed a rich variety of features including one,- two- and three-dimensional diffuse scattering, as well as incommensurate satellites. At the centre and one tip of the crystal the symmetry appears to be orthorhombic, whereas at the other tip the symmetry of the satellites and of some of the diffuse scattering is clearly monoclinic, indicating that the crystal is not homogeneous. Most of the scattering could be assigned to *R*/*S* occupational disorder of the chiral host molecules, to positional disorder of the guest molecules or to local distortions of the average structure. Assignments are based on the disorder deduced from the average structure and the molecular form factors of host and guest molecules which show characteristic patterns in reciprocal space. Two smaller, orthorhombic twin fragments and an additional phase with hexagonal symmetry have also been found.

1. Introduction

Inclusion compounds of racemic perhydrotriphenylene (PHTP) tend to be heavily disordered and show an extraordinary richness of complex and sometimes unusual diffraction features, including incommensurate satellites as well as one-, two- and three-dimensional diffuse scattering (König *et al.*, 1997; Mayo *et al.*, 1999). In this paper all non-Bragg scattering observed for the PHTP inclusion compound with 1-(4-nitrophenyl)piperazine (NPP) is described and classified; the various features are assigned to the host and guest molecules and qualitative interpretations of the observations are proposed.

Our motivation to study PHTP inclusion compounds is threefold: first they combine substructures of different dimensionality and symmetry (see §2). This raises interesting questions about the energetic interactions of the substructures and their crystallographic consequences. Second, inclusion compounds of the racemic host PHTP with polar guest molecules are themselves polar. They are well suited for studies in crystal engineering, *e.g.* for controlling the degree of parallel alignment of non-linear optic molecules (Hulliger *et al.*, 1995; Hoss *et al.*, 1996). A detailed understanding of the interactions within and between host and guest substructures is a key for tuning the properties of the composite structure (Hulliger *et al.*, 2000). Third, in the presence of disorder and

modulations, the structural model of a crystal derived from Bragg reflections represents the space and time average which provides incomplete information on the molecular architecture and the molecular interactions on a local scale. Deviations from the regularity of the three-dimensional average structure, including their short- and long-range order, are reflected in the diffuse and satellite intensities. Analysis of these phenomena is a challenge by itself and may be a fruitful source of information on the principles of supramolecular self-organization in molecular crystals.

This paper is organized as follows: §2 gives a summary of previous work. Details of the diffraction experiments performed on the inclusion compound $PHTP_5$·NPP are reported in §3. §4 describes observed diffraction features and presents tentative models for their interpretation. §5 summarizes our conclusions.

2. Summary of previous work

The basic crystal architecture of PHTP inclusion compounds has been investigated by Farina and co-workers (Farina, 1984; Farina *et al.*, 1997) for a number of included guest molecules. They found that stacks of triangular PHTP molecules form a honeycomb-like arrangement of tunnels into which the guest molecules are embedded. The general structure is similar to that shown in Fig. 1, in which one-dimensional chains of guest molecules are included in the tunnels of a three-dimensional framework of host molecules. The guest molecules are always heavily disordered and thus only the projection of the structures onto the **ab** plane could be determined easily. Mayo *et al.* (1999) investigated the diffuse scattering from the PHTP inclusion compound with cyclohexane. The $\bar{3}$ axes of the cyclohexane molecules in the tunnels are perpendicular to the tunnel axis and show hexagonal orientational disorder with respect to **c** (Allegra *et al.*, 1965). By analysing the diffuse intensities in the *hk*0 layer with the help of Monte Carlo methods, Mayo *et al.* (1999) could show that the orientations of the cyclohexane molecules are correlated between neighbouring tunnels. As a consequence, the hexagonal host lattice is distorted and locally the symmetry is reduced to monoclinic.

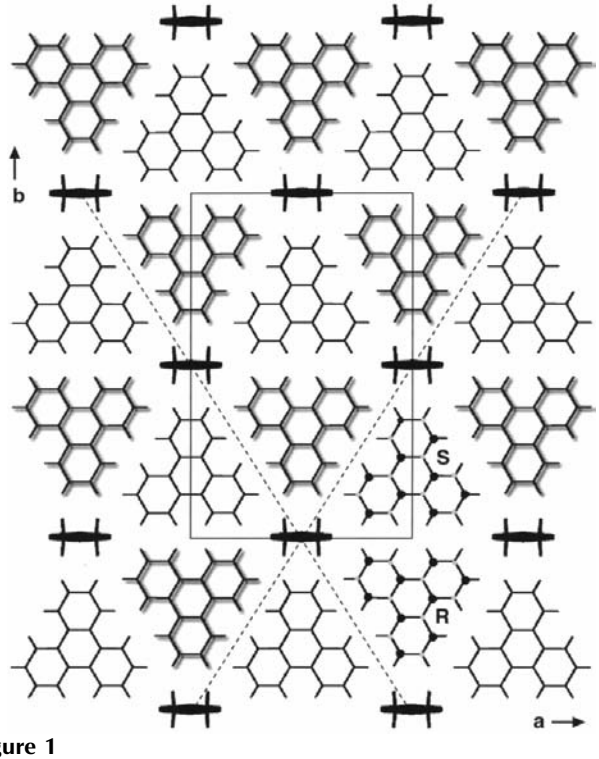

Figure 1
The structure of the $PHTP_5$·NPP inclusion compound as viewed down the **c** axis. Different z positions of PHTP molecules are indicated by shadowed ($z = 0.75$) and non-shadowed ($z = 0.25$) surroundings. The wavy shape of an *R* and an *S* molecule is shown at the bottom right. C atoms above the molecular mean plane are shown by black atoms, those below by grey ones. The solid rectangle indicates the C-centred unit cell. The dashed lines indicate interfacing planes between twin domains.

Table 1
Some experimental parameters.

Data set	1	2	3	4	5
Crystal location	Free tip	Centre	Glued tip	Free tip	Centre
Beam width perpendicular **c** (mm)	0.5	0.5	0.5	0.5	0.5
Beam width parallel **c** (mm)	0.25	0.1	0.1	0.1	0.1
2θ max. (°)	41.6	41.6	41.6	41.6	41.6
Total rotation range (°)	180	180	50.6	180	119.6
No. of frames	900	900	253	900	598
Temperature	RT†	RT†	RT†	120 K	120 K
λ (Å)	0.7500	0.7501	0.7501	0.7501	0.7501
Synchrotron mode	Single bunch	16 bunch	16 bunch	16 bunch	16 bunch

A complete three-dimensional average structure was determined for the inclusion compound of racemic PHTP with NPP as a guest molecule (König *et al.*, 1997). Due to the near flatness of the guest molecules the tunnels are narrower along **b** than along **a** and the PHTP framework is distorted to an orthorhombic C-centred arrangement. The average host and guest sublattices are both heavily disordered. Every host site is occupied by half an *R*-PHTP and half an *S*-PHTP molecule[1] (Fig. 1). From the translation distance $|\mathbf{c}_h|$ of the host stacks König *et al.* (1997) and Farina (1984) deduced that individual stacks are built from homochiral PHTP molecules. *R* and *S* stacks were assumed to be distributed randomly in the **ab** plane. Consecutive guest molecules within one tunnel are related by a *c*-glide plane perpendicular to **b**, so that the translation distance $|\mathbf{c}_g|$ of the guest within one tunnel is twice the length of a single guest molecule. It is commensurate with the translation period $|\mathbf{c}_h|$ of the host structure ($|\mathbf{c}_h|:|\mathbf{c}_g| = 1:5$). The guest molecules in neighbouring tunnels are parallel (rather than antiparallel) and disordered over five positions which are strongly correlated with the host structure: Their z coordinates differ by $\Delta z_h = -2, -1, 0, 1$ or 2 unit cells of the host, and each of the five positions is occupied with a prob-

[1] PHTP molecules are chiral. According to the nomenclature given by Cahn *et al.* (1966) and Prelog & Helmchen (1982) they are designated as *R*,*R*,*R*,*R*,*R*- and *S*,*S*,*S*,*S*,*S*-PHTP. For the sake of simplicity this has been abbreviated to *R*-PHTP and *S*-PHTP.

ability of 0.2. This reduces the apparent translation of the average guest structure in the **c** direction to $|\mathbf{c}_g| = |\mathbf{c}_h|$. Although the unit-cell dimensions of the two average substructures are the same, their symmetries are different – *Cmcm* for the host and $Cmc2_1$ for the guest.

The finding that the polar guest molecules in neighbouring tunnels point in the same direction, *i.e.* the formation of a macroscopically polar guest structure, was surprising for two reasons: first, the average host structure is centrosymmetric and, second, there is no direct contact between the guest molecules in adjacent tunnels which are ∼14–15 Å apart. An indirect interaction between the guest molecules *e.g. via* a modulation of the tunnel walls, was judged improbable because of the small size of the atomic mean square displa-

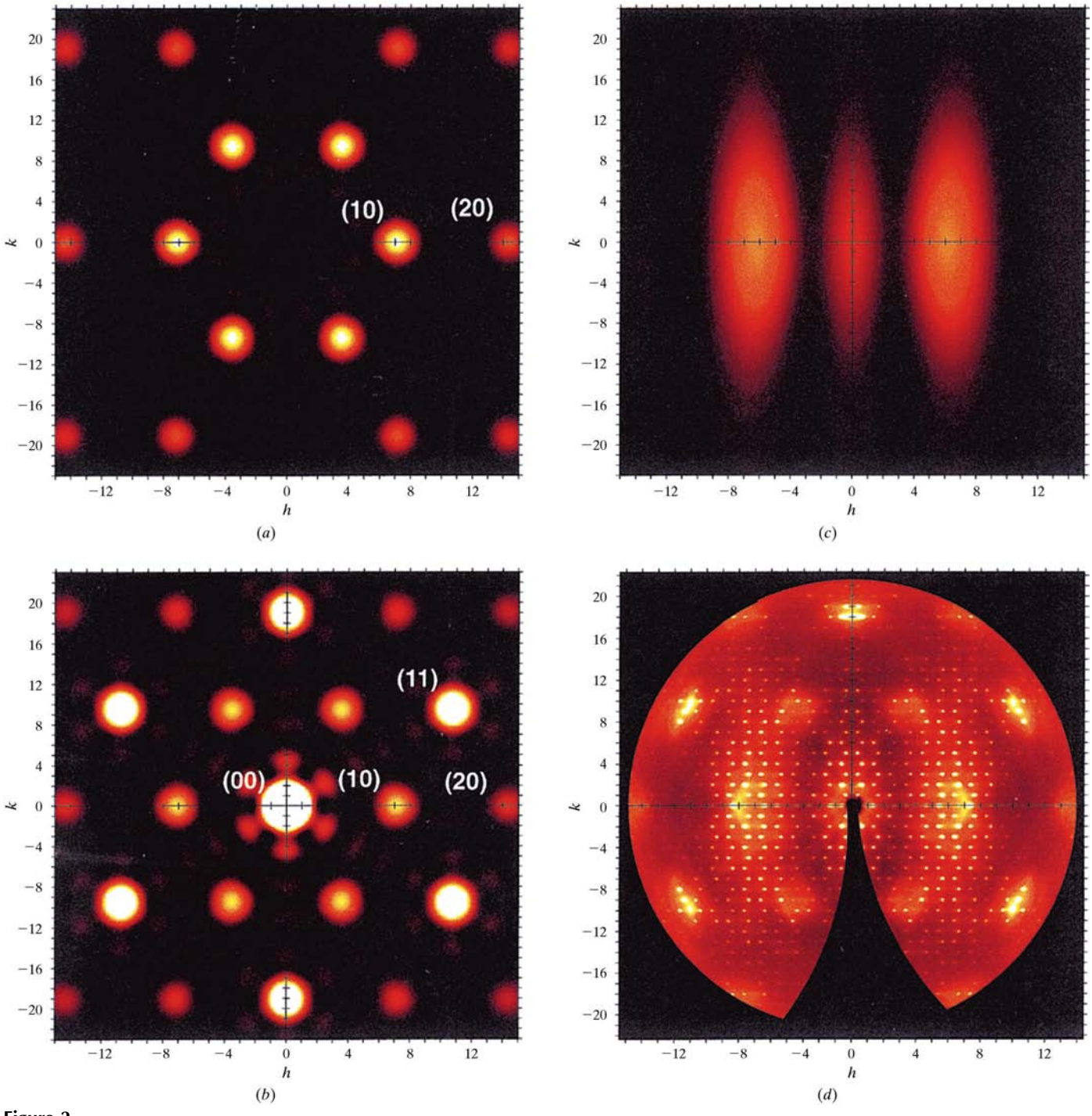

Figure 2
Molecular form factors: (*a*) $|\Delta f_{\rm PHTP}|^2 = |0.5(f_R - f_S)|^2$ at *hk*2 corresponding to the subtractive superposition of an *R*- and an *S*-PHTP molecule; (*b*) $|\bar{f}_{\rm PHTP}|^2 = |0.5(f_R + f_S)|^2$ at *hk*2 corresponding to the additive superposition of an *R* and an *S*-PHTP molecule (numbers in brackets are indices of a hexagonal system of columns parallel to **c***, see text); (*c*) $|f_{\rm NPP_2}|^2$ of an NPP_2 motif at *hk*1.2 (all at the same intensity scale); (*d*) *hk*1.2 layer from the crystal centre (room temperature).

cements in the **ab** plane. Instead, the polar arrangement of the guest molecules has been explained in terms of a Markov model of crystal growth (König *et al.*, 1997): if the interaction energies $-NO_2\cdots HN-$, $-NH\cdots HN-$ and $-NO_2\cdots O_2N-$ between consecutive NPP guest molecules $HN(CH_2-CH_2)_2N-C_6H_4-NO_2$ in a tunnel are different, the growth process leads to a parallel arrangement of the NPP molecules in the growing tunnels and thus to polar needle-like crystals.

König *et al.* (1997) have observed diffuse and satellite scattering on consecutive layers perpendicular to **c*** with a spacing corresponding to the length of two guest molecules, $|\mathbf{c}_g|$. They assigned the diffuse scattering to the positional disorder of the guest molecules. The satellite reflections on the diffuse layers were taken to indicate that the differences Δz of the positions of the guest molecules in different channels show long-range correlation also in the **a** and **b** directions; no detailed or quantitative model was provided for these observations.

3. Experimental

3.1. Sample preparation and selection

Crystals of $PHTP_5\cdot NPP$ were grown as described by König *et al.* (1997). Transparent, needle-like, prismatic specimens without visible fluid inclusions or intergrowth were selected and mounted parallel to a glass fibre at one tip. The capping faces of the crystals are irregular and rough. Thus, it was not always easy to distinguish terminal faces formed during crystal growth from crystal tips which have been broken by handling, or from tips which have been in contact with the container during crystallization. Two crystals have been examined using Weissenberg/oscillation and step-scan techniques. The crystal used in the Weissenberg experiment was ∼4 mm long and ∼1 mm wide. It showed rough, but approximately pyramidal, faces at its free tip, which can be assumed to be terminal faces from crystal growth. The tip mounted to the glass fibre seemed to be fractured. The crystal used in the synchrotron experiments was ∼2.5 mm long and ∼0.4 mm in diameter. It showed one very smooth face at its free tip, an indication that it was in

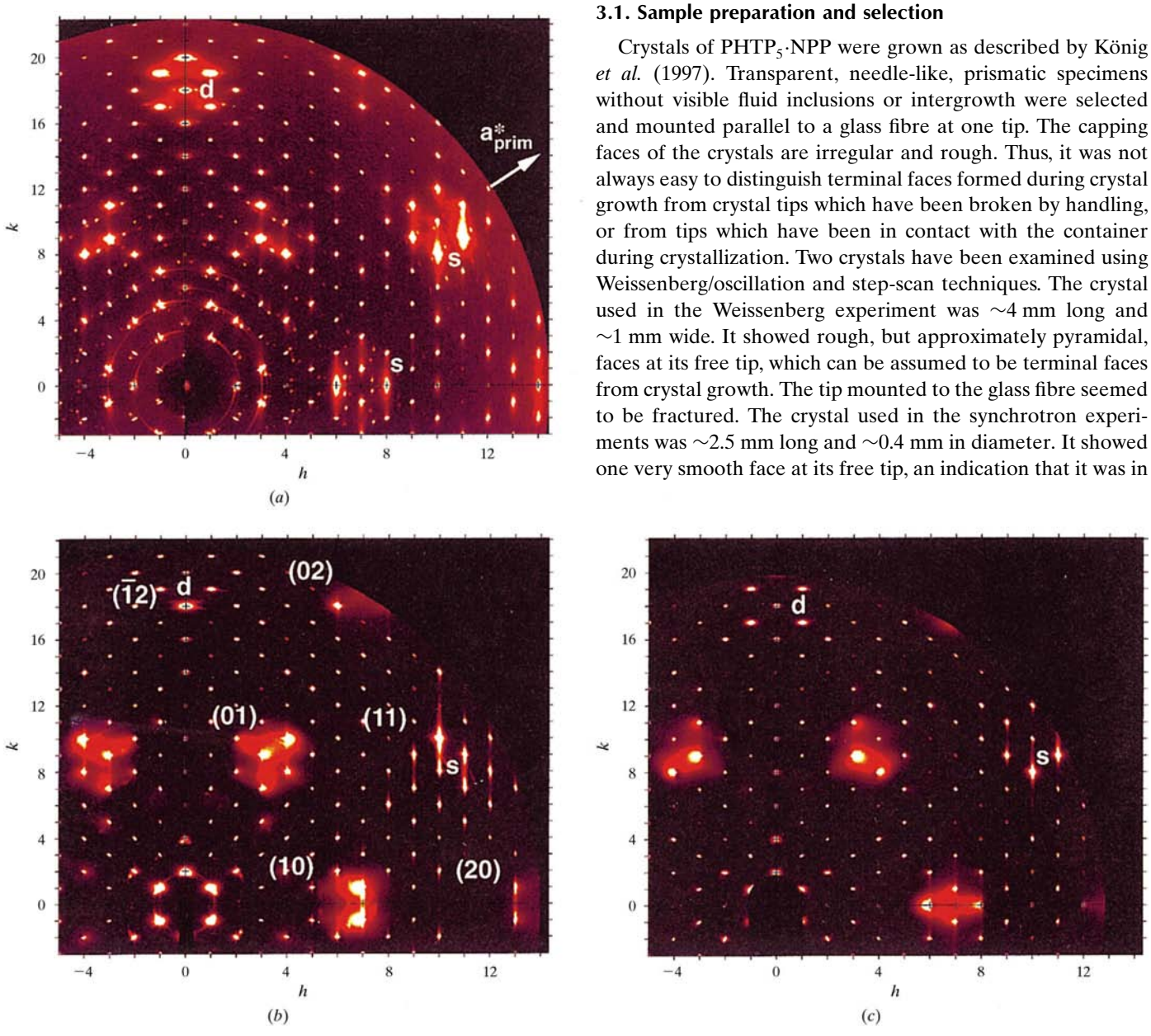

Figure 3
Bragg layers from the free tip. Intensities are on about the same scale. Representatives of the disc-like scattering perpendicular to **b*** and the streak-like scattering parallel to **b*** are labeled by 'd' and 's', respectively. Note the high signal-to-noise ratio in (*b*) and (*c*). The higher background in (*a*) is not diffuse scattering, but due to the lower beam intensity of single bunch mode (see Table 1). (*a*) *hk*0 (room temperature). There is no broad diffuse scattering in the regions of columns (10) and (20). Ring-like intensities close to the origin can be assigned to incomplete erasure of highly over-exposed reflections. They remain visible in several successive image plate frames. (*b*) *hk*1 (120 K). Diffuse columns (10) are clearly visible. Broad diffuse scattering from columns (11) is too weak to be seen. Note the minor deviations from mirror symmetry between the broad diffuse columns (01) and $(\bar{1}1)$. (*c*) *hk*2 (120 K). Note that the broad diffuse features in the columns (10) are strong at positions where they are weak in *hk*1 and *vice versa*.

contact with the container during crystal growth. However, it is not clear whether this tip contains the crystal's seed or, whether crystal growth was terminated at this point by touching the container wall. The second tip of this crystal was clearly fractured.

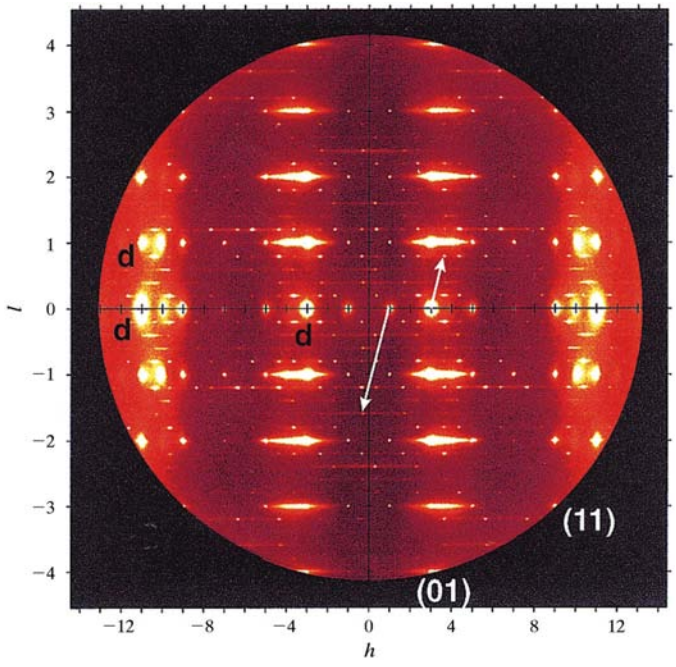

Figure 4
The *h*9*l* layer from the free tip (room temperature). Horizontal lines at $|h| = 2$–5 show the condensation of intensity of the columns (10) into the Bragg layers (§4.2.1). Corresponding intensities between Bragg layers are very weak. The columns (11) can be seen between $|h| = 9$ and 11 (§4.2.2). The ellipsoidal diffuse intensities in the columns (11) are cross sections through the streak system parallel to **b*** (§4.3.1). Diffuse disc-like scattering is superimposed on the Bragg reflections, *e.g.* on the 190, 390 and 590 reflections. Arrows indicate the first-order satellite vector (0.64, 0, 0.8) and the second-order satellite vector (−1.28, 0, −1.6). Representative disc-like diffuse scattering is labeled by 'd'.

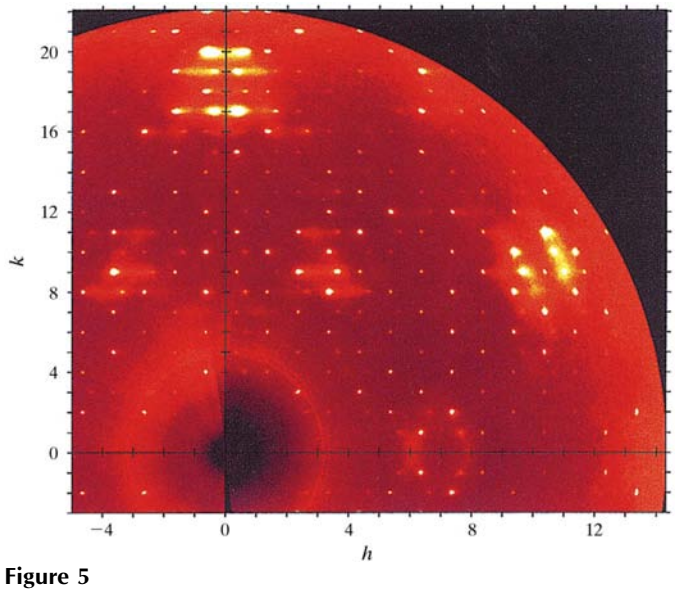

Figure 5
The *hk*0.2 layer from the free tip (120 K), see text.

3.2. Oscillation and Weissenberg experiments

Room-temperature oscillation and Weissenberg photographs of the first crystal were recorded using filtered Cu $K\alpha$ radiation with a beam diameter of 0.8 mm. The pictures, including those from higher layers, were taken in normal beam mode, in order to assure that always the same slice of material was exposed to the beam. Weissenberg photographs of layers perpendicular to **c*** were taken at $l_h = 0, 0.2, 0.4, 0.8, 1, 1.2, 1.6, 2$ at the crystal centre and at the glued tip. One photograph with $l_h = 1.2$ was taken from the free tip. In addition, oscillation photographs were taken from the centre and from both tips. At the centre of the crystal the exposure time was 72 h for

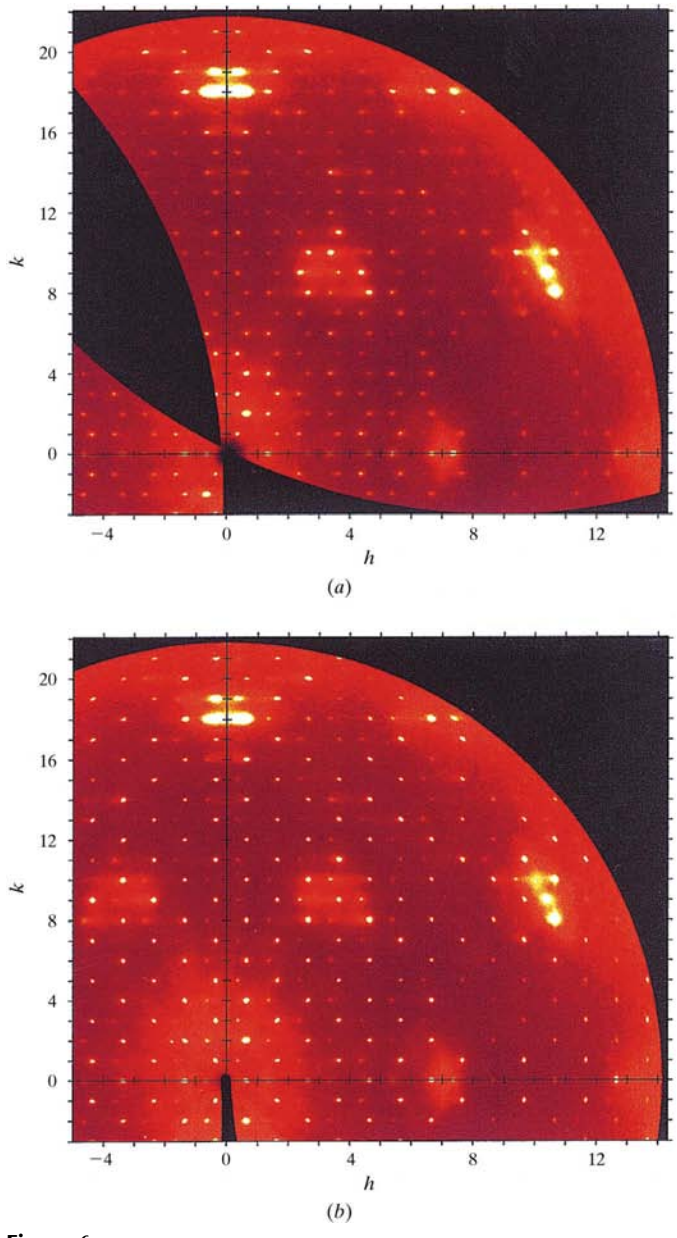

Figure 6
(*a*) The *hk*0.8 layer from the crystal centre (120 K). Satellites and diffuse intensities show approximate *mm* symmetry. (*b*) The *hk*0.8 layer from the free tip (120 K). Note that the *mm* symmetry of the satellite intensities but not of the diffuse intensities is broken. Intensities are on about the same scale.

the diffuse layers (l_h = 0.2, 0.4, 0.8, 1.2, 1.6) and 48 h for the Bragg layers (l_h = 0, 1, 2). At the tip of the crystal, the exposure time was 72 h for all experiments. The oscillation range was 180° for all photographs.

3.3. Synchrotron experiments

Five data sets of the second crystal were measured in two runs at the Swiss–Norwegian beam-lines (SNBL) located at the European Synchrotron Radiation Facility, Grenoble, France (Table 1). Data set 1 was measured in the first experiment (1 d), while data sets 2–5 were measured in the second experiment (4 d). The same crystal was used for all measurements. The incident beam was normal to the spindle axis of the single circle goniometer and to the planar image plate (MAR research image-plate detector system 345 mm). The following settings were chosen:

Needle axis **c** parallel to the oscillation axis.

Horizontal slits on the primary beam side to select the irradiated crystal volume; vertical slits set to irradiate the full diameter of the needle-shaped crystals (Table 1). This procedure avoids cutting the crystal into pieces and ensures that the

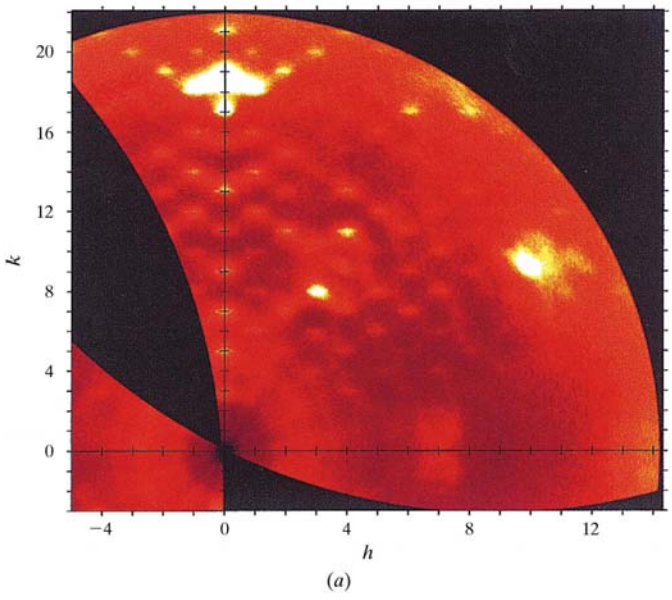

Figure 7
(*a*) The *hk*0.6 layer from the crystal centre (120 K). Streak-like diffuse intensities can be observed along **a*** interconnecting *positions* of second-order satellite reflections from different twin domains. Note that satellite reflections are not observable. (*b*) The *hk*0.6 layer from the free tip (120 K). Satellite reflections of one twin domain are clearly present. Intensities are on about the same scale.

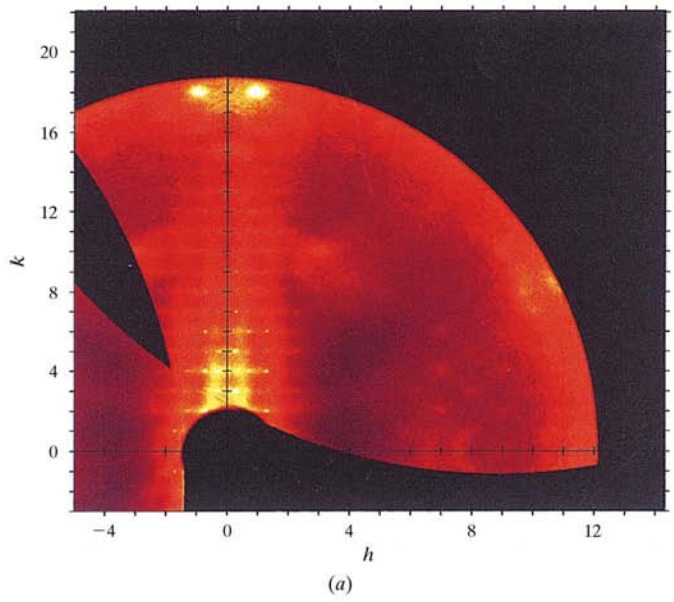

Figure 8
(*a*) The *hk*2.4 layer from the crystal centre (120 K). Diffuse intensities form a pseudo-rectangular lattice. (*b*) The *hk*2.4 layer from the free tip (120 K). Note that diffuse scattering is triangle-like, connecting second-order satellites. Note also that satellite intensities are much stronger than at the crystal centre, especially at high *h*. Intensities are on about the same scale.

Table 2
Lattice parameters as obtained by the program XDS.

Data set	1	2	3	4	5
Crystal location/ temperature	Free tip, RT†	Centre, RT†	Glued tip, RT†	Free tip, 120 K	Centre, 120 K
a (Å)	15.173 (< 1)	15.163 (1)	15.151 (5)	15.054 (3)	15.059 (1)
b (Å)	23.491 (1)	23.491 (2)	23.484 (4)	23.237 (5)	23.235 (1)
c (Å)	4.779 (1)	4.779 (1)	4.777 (1)	4.715 (1)	4.713 (1)
α (°)	90	90	90	90	90
β (°)	90	90	90	90	90
γ (°)	90	90	90	90	90

† RT = room temperature.

exposed crystal volume is the same for all rotation angles. A disadvantage is that no information about diffraction features close to **c*** is available, as this region is always outside the Ewald sphere. Using slits on the primary beam optimizes resolution in selecting the crystal volume and narrows the resolution function along **c***. The latter point is important because Weissenberg and oscillation experiments have indicated that the intrinsic width of many diffuse diffraction features may be small along **c***.

The crystal-to-detector distance was 135 mm and $(\sin\theta/\lambda)_{\max} = 0.47$ Å^{-1}. This made it possible to record the two inner-most features of a pseudo-hexagonal system of diffuse columns oriented parallel to **c*** in the range $-2 \le l_h \le 2$ (§4.2). The exploratory Weissenberg experiments had shown this feature to be dominant throughout.

Overall rotation range of 180° to ensure complete information on symmetry and some redundancy (due to limited time experiments 3 and 5 were incomplete, see Table 1).

Rotation range per frame of 0.2° to ensure a high resolution tangential to the rotation axis.

Exposure times of ∼1 min per frame to ensure highly significant intensities of all diffuse diffraction features identified on Weissenberg or oscillation photographs. The exact exposure time was dependent on primary beam intensity ('dose mode').

The read-out diameter of the image plate was 240 mm, pixel size 150 µm. This resulted in a read-out time of ∼50 s per frame.

Measurements at room temperature and at 120 K to separate dynamic from static disorder.

3.4. Data processing

The raw data were transformed into reciprocal space units using the program package *XCAVATE* (Estermann & Steurer, 1998; Scheidegger *et al.*, 2000), which reconstructs the differential cross section $\delta\sigma/\delta\Omega$ of the diffuse scattering in arbitrary layers or volumes of reciprocal space from a single series of successive rotation images. Crystal orientation, lattice constants and instrumental parameters are needed for the reconstruction. They were refined from the positions of Bragg reflections in detector space using the program package *XDS* (Kabsch, 1993). The algorithm used by *XDS* has been described in detail by Kabsch (1988*a*,*b*, 1993). Refined lattice parameters are shown in Table 2. Note that crystal orientation is determined from the diffraction data after the measurement, *i.e.* no pre-alignment of the crystal is required. Other important input for the program *XCAVATE* includes the definition and grid size of the desired reciprocal sections and information on polarization corrections. A scale factor must be supplied for each frame to correct primary beam fluctuations determined from background scattering (program *BACKGROUND*, which is part of the *XCAVATE* program package). A detailed description of the scaling procedure can be found in Estermann & Steurer (1998). The success of the procedure is apparent from the smoothness of the reconstructed pictures (Figs. 2*d* and 3–8).

Layers were calculated perpendicular to the orthorhombic crystal axes with a grid size of 0.001 Å^{-1} (*xkl* layers with $x = 0$, 0.25, 0.5..., 10, 10.5, 11, 11.5..., 14; *hxl* layers with $x = 0$, 1, 2, 3..., 14; *hkx* layers with $x = 0$, 0.1, 0.2, 0.3..., 1.6, 1.8, 2, 2.2..., 3.2). The intensity profiles of the diffuse part of the *hkx* layers are very narrow along **c*** and thus, small errors in the orientation matrix can lead to spurious variations of intensities in the reconstructed layers. To avoid this, intensities of *hkx* layers (with $x = 0.2$, 0.4, 0.6, 0.8, 1.2...) were obtained by integrating over a range of ± 0.0025 Å^{-1} along **c***. For all other layers, the resolution perpendicular to the layer was set to 'zero', *i.e.* to the optimum defined by the chosen rotation range per frame and by the pixel size of the detector (§3.3). *hkx* layers with $x =$ 0.2, 0.4, 0.6, 0.8, 1.2... (l_h = non-integer) are called satellite layers; layers with integer l_h and containing only Bragg but no satellite reflections are referred to as Bragg layers.

A total of 5 Gbytes of raw data was transformed into ∼400 reconstructed layers representing ∼6 Gbytes of data. The procedure took approximately 4 d of CPU time on a Silicon Graphics Indigo 2 work station, *i.e.* about the same time as data collection.

4. Observations and interpretations

4.1. Molecular form factors, a basis for analysis and interpretation

In this section we ask where in reciprocal space the most prominent non-Bragg intensities may be expected given the disorder deduced from the average structure, especially the racemic disorder of the host and the positional disorder along the tunnel axis of the guest. An answer is relatively easy because the relevant form factors of host and guest molecules show characteristic maxima in different parts of reciprocal space and a special orientation with respect to the crystal axes.

The PHTP host molecule shows almost perfect 32 symmetry; in the average structure the mean molecular planes of the superimposed *R*- and *S*-PHTP molecules coincide leading to a pseudo-molecular building block with approximate point symmetry $\bar{6}2m$. The $\bar{6}$ axis is parallel to **c** and one

twofold axis is parallel to **b** (Fig. 1). The two pseudo-molecules in the primitive unit cell are related by an inversion centre.

The form factor of the pseudo-molecule with electron density $\overline{\rho}_{\rm PHTP} = 0.5(\rho_R + \rho_S)$ is $\overline{f}_{\rm PHTP} = 0.5(f_R + f_S)$, where f_R and f_S denote the Fourier transforms of ρ_R and ρ_S, respectively. Since a given site is occupied by either an *R or* an *S* molecule, there are local deviations $\Delta\rho_{\rm PHTP} = \pm 0.5(\rho_R - \rho_S)$ from the average density $\overline{\rho}_{\rm PHTP}$; the positive sign implies an *R*-PHTP, the negative sign an *S*-PHTP molecule on the given site. The corresponding difference form factor is $\Delta f_{\rm PHTP} = \pm 0.5(f_R - f_S)$. The scattering powers of the difference and of the average electron densities $|\Delta f_{\rm PHTP}|^2$ and $|\overline{f}_{\rm PHTP}|^2$ are shown in Figs. 2(*a*) and (*b*). $|\overline{f}_{\rm PHTP}|^2$ is concentrated into columns forming a hexagonal two-dimensional lattice with a spacing of ~ 2.5 Å, corresponding to the distance between the ring centres of the host molecule. The columns run parallel to **c***, *i.e.* normal to the molecular plane of the relatively flat PHTP molecules. The spots in Fig. 2(*b*) are cross-sections through these columns. $|\Delta f_{\rm PHTP}|^2$ is based on the same hexagonal lattice as $\overline{f}_{\rm PHTP}$, but exhibits special extinctions: only columns with indices (10) and (20) are present, while columns with indices (00) and (11), which are strongest in $\overline{f}_{\rm PHTP}$, are absent here (Fig. 2*a*). In the *hk*0 layer $|\Delta f_{\rm PHTP}|^2$ is zero everywhere, because in projection down **c** $\Delta\rho_{\rm PHTP}$ is zero everywhere. Two important conclusions follow:

(i) all diffuse intensities arising from or related to *R*/*S* occupational disorder are governed by $\Delta f_{\rm PHTP}$ and are especially strong in columns (10) and (20); the *hk*0 layer and columns (00) and (11) contain no information on *R*/*S* disorder;

(ii) conversely, diffuse or satellite scattering arising from displacive or librational disorder of the host which is not associated with *R*/*S* disorder and affects *R* and *S* molecules equally, is governed exclusively by $\overline{f}_{\rm PHTP}$ and is especially strong in columns (00) and (11).

The hexagonal patterns of the average and difference form factor amplitudes are the same for both PHTP molecules in the primitive unit cell, because of their particular orientation relative to each other and relative to the crystal axes. Spatial correlations between the two sites will thus not change the general appearance of non-Bragg intensities, but may modulate them (Welberry & Butler, 1995). The modulations are broad if the average correlation length is small; they degenerate into sharp reflections if the correlation length is very large.

The NPP guest molecules may be discussed in a similar way. The long axis of the molecule is almost parallel to **c** with which it forms an angle of only 4°. The molecules are relatively flat along **b**. Two consecutive NPP molecules are related to each other by a *c*-glide plane perpendicular to **b**. They form the translational motif which extends over five unit cells of the host. The motifs in different channels are displaced by $\Delta z = -2, -1, 0, 1$ or 2 unit cells of the host and each position is occupied with a probability of 0.2. Thus, the average guest structure is built from a pseudo-molecule with length $|\mathbf{c}_h|$ and electron density $\overline{\rho}_{\rm NPP_2} = 0.2(\rho_{\rm NPP_2}(\Delta z_h = -2) + \rho_{\rm NPP_2}(\Delta z_h = -1) + \rho_{\rm NPP_2}(\Delta z_h = 0) + \rho_{\rm NPP_2}(\Delta z_h = 1) + \rho_{\rm NPP_2}(\Delta z_h = 2))$, where $\rho_{\rm NPP_2}$ is the electron density of an NPP_2 motif. The form factor of this pseudo-molecule is $\overline{f}_{\rm NPP_2} = 0.2 f_{\rm NPP_2}(1 + 2\cos(2\pi l_h) + 2\cos(2\pi 2 l_h))$ with $f_{\rm NPP_2}$ being the Fourier transform of $\rho_{\rm NPP_2}$. Within a given channel only one of the five possible z positions may be occupied by an NPP_2 motif and thus the local deviation from the average density may be written as $\Delta\rho_{\rm NPP_2} = \rho_{\rm NPP_2} - \overline{\rho}_{\rm NPP_2}$. The difference form factor is $\Delta f_{\rm NPP_2} = f_{\rm NPP_2} - \overline{f}_{\rm NPP_2} = 0.2 f_{\rm NPP_2}(4 - 2\cos(2\pi l_h) - 2\cos(2\pi 2 l_h)) e^{2\pi i l_h z_0}$ with z_0 representing a particular z-position of the motif. $\overline{f}_{\rm NPP_2}$ becomes f_{NPP_2} at integer l_h and is zero at $|l_h| = 0.2, 0.4, 0.6, 0.8, 1.2...$, *i.e.* at positions of the satellite layers, while $\Delta f_{\rm NPP_2}$ is zero at positions of Bragg layers and becomes $f_{\rm NPP_2} e^{2\pi i l_h z_0}$ at positions of satellite layers. The form factor of the NPP molecules shows broad bands which extend along **b***, are broad and somewhat modulated along **a*** and narrow along **c***. As an example, the section *hk*1.2 of $f_{\rm NPP_2}$ is shown, a layer in which $f_{\rm NPP_2}$ is particularly strong (Fig. 2*c*). Owing to the *c*-glide plane perpendicular to **b**, the NPP_2 form factors vanishes at $k = 0$ for $|l_h| = 0.2(2n + 1)$ (n = integer).

It is relatively easy to separate disorder scattering due to guest and host molecules, because the relatively narrow columns characteristic of the host are parallel to **c*** whereas the broad bands characteristic of the guest extend along **b***. The *hk*1.2 layer shows nicely that strong guest scattering may occur at positions where the host scattering is almost zero and *vice versa* (Fig. 2*d*; compare with Figs. 2*a*, *b* and *c*).

4.2. Diffuse columns

A system of diffuse columns running parallel to **c*** is apparent in all data sets (Figs. 3*a–c* and 4). The columns with indices (10) and (11) and part of the columns (20) are present in layers *hk*0, *hk*1 and *hk*2. Due to the 1 Å resolution limit only the first-order columns (10) are observable in the *hk*3 layer. The zero-order column (00) can be seen only in the neighbourhood of the *hk*1 layer; everywhere else it is hidden by the beam-stop or falls into the blind region arising from the normal-beam diffraction geometry. In the Bragg layers, diffuse streak-like scattering perpendicular to **a*** and disk-like scattering perpendicular to **b*** is superimposed on the columns. In contrast to the three-dimensional column system, these features are approximately one- and two-dimensional and will be described in §4.3.

Based on their positions in reciprocal space, the columns can uniquely and exclusively be assigned to scattering from the PHTP molecules (Figs. 2*a* and *b*). The intensity distributions in columns (10) and (20), which are mainly governed by $\Delta f_{\rm PHTP}$, are quite different from those in the columns (00) and (11), which are governed by $\overline{f}_{\rm PHTP}$.

4.2.1. Columns (10), (01), (20) and (02). Intensity profiles along **c*** show pronounced maxima centred on the Bragg layers with $|l_h| = 1, 2$ and 3; their half-width is ~ 0.1 in units of l_h and the profiles are slightly asymmetric. Column intensities are very weak between Bragg layers (Fig. 4). This indicates that the chirality of PHTP molecules along **c** tends to be the same. The average correlation length is ~ 10 unit cells, in agreement with the assumption of König *et al.* (1997) that PHTP stacks are homochiral. In the *hk*0 layer, diffuse scat-

tering on the columns (10) and (20) is almost completely absent, as expected from $\Delta f_{\rm PHTP}$ (Fig. 3*a*).

In and close to Bragg layers with $l_h \neq 0$ the columns display broad modulations with complex, irregular shapes extending into weak side maxima around the Bragg positions 421, 351 and 161 (Fig. 3*b*), which are also compatible with $\Delta f_{\rm PHTP}$ (Fig. 2*a*). No significant temperature dependence has been found. The modulations indicate that the distribution of *R* and *S* molecules is also correlated in lateral directions, in contradiction to König *et al.* (1997) who assumed a random distribution of homochiral stacks.

Close to the Bragg positions the broad modulations develop into strong, relatively narrow maxima which are distinctly asymmetric along **a***. There is an intensity minimum close to the Bragg positions which is even lower than the diffuse average described in the preceding paragraph (see *e.g.* dark shadows close to reflections 602 and 482 in Fig. 3*c*). The minimum becomes more pronounced at low temperature. The asymmetric profiles are visible primarily on columns (10) and to some extent also on (20), but not on (11). From the literature it is known that occupational disorder associated with displacive disorder can lead to asymmetric profiles around Bragg reflections (Welberry & Butler, 1994). In analogy, we suggest that the narrow asymmetric features indicate some kind of displacive disorder associated with *R*/*S* disorder.

4.2.2. Columns (00), (11) and ($\bar{1}$2). The intensities of the columns (11) within Bragg layers are generally weaker than for columns (10) and (20), whereas the reverse is true between Bragg layers. There are no narrow maxima where the columns pass through Bragg layers (Fig. 4). With increasing $|l_h|$, the integral intensities decrease more or less continuously. Columns (11) are weak but clearly visible within the *hk*0 layer, even against the much stronger streaky pattern (Fig. 3*a*). These modulations differ from those of columns (10) not only along **c***, but also in the **a*****b*** planes. Apart from the streaky and disc-shaped features centred at Bragg positions (§§4.3.1 and 4.3.2) there is a diffuse background with broad maxima which are somewhat wider in tangential directions than in radial directions. This is best seen in the ($\bar{1}$2) column (Fig. 3*a*). The broad diffuse background exhibits a minimum at $k \simeq 18.5$, which extends along **a***. Between the Bragg layers, columns (11) show similar, but less pronounced modulations as within Bragg layers. As far as observable, column (00) exhibits no broad diffuse intensities. At low temperature, intensities of columns (11) become significantly weaker relative to those of columns (10). This is a clear indication that these diffuse intensities are due largely to some dynamic disorder of the host.

4.2.3. Features common to all columns. The (10), (20) and (11) families of columns all show broad local maxima within and close to layers *hk*0 and *hk*2 matched by corresponding minima within and close to layers *hk*1 and *hk*3, and *vice versa*. (*cf.* Figs. 3*a* and *c* with Fig. 3*b*). Midway between the Bragg layers at *hk*0.5, *hk*1.5 and *hk*2.5, almost no modulation of the diffuse columns is visible. Modulations of columns are of approximately orthorhombic symmetry. Very small intensity variations of columns (10) break the **a*****b*** and **b*****c*** mirror planes and reduce the symmetry to a twofold axis along **c*** (Figs. 3*b* and *c*). All features described above are very similar at the two crystal tips and at its centre.

4.3. Other scattering in the Bragg layers

4.3.1. Streak-like scattering parallel to b*. A system of streaks parallel to **b*** can be observed in all Bragg layers (Figs. 3*a*–*c*; labels 's'). Generally, the streaks are most intense on the diffuse columns (11) at large $|h|$, but too weak to be seen close to $h = 0$. The intensities are strongest at $l_h = 0$ and decrease with increasing $|l_h|$. At room temperature the streaks are not completely sharp along **a*** and **c***; at 120 K they become significantly sharper. The average length of the streaks is $\sim 2|\mathbf{b}^*|$, their intensities are highest close to Bragg positions. Intensity profiles along **b*** are more or less independent of temperature. The pattern is very similar for all crystal locations.

Diffuse systems showing increasing intensities in a particular direction of reciprocal space represent displacive disorder with small amplitudes. Systematic absences in lines or planes perpendicular to this direction and passing through the origin of reciprocal space imply that the displacements are not visible in the corresponding projections in real space and must therefore coincide with the direction of projection. In $PHTP_5$·NPP the streaks are stronger in columns (11) than in ($\bar{1}$2) and absent in the 0*kl* layer, implying that (i) streak intensities appear to be governed by $\overline{f}_{\rm PHTP}$ and (ii) the displacement must be perpendicular to 0*kl*, *i.e.* along **a**. The small widths of the streaks in directions perpendicular to **b*** indicate that correlation lengths are quite large parallel to **a** and **c**, but short along **b**. With decreasing temperature, correlation increases along **a** and **c**, while it is almost unchanged along **b**. Taken together these observations imply extended shear deformations in the **ac** plane, whose shear components along +**a** or −**a** are only weakly correlated from host layer to host layer (*i.e.* along **b**, Fig. 1). The shear displacement affects *R*- and *S*-PHTP molecules equally and deforms the H···H intermolecular contacts in the **ac** plane from the 'head-on' arrangement shown in Fig. 1 towards a 'staggered' arrangement akin to that seen along **a**. The change in H···H contacts may well provide the driving force for the deformation. The system of streaks described here is similar to a streak-like pattern observed in the PHTP/cyclohexane inclusion compound (Mayo *et al.*, 1999). There it was explained by a monoclinic distortion of the average host lattice which is hexagonal.

4.3.2. Disc-like scattering perpendicular to b*. Diffuse scattering of disc-like shape surround Bragg positions symmetrically. The discs are quite narrow along **b*** and somewhat broader in the **a*****c*** layers (Figs. 3 and 4; labels 'd'). To a first approximation, intensities are proportional to those of attendant Bragg reflections everywhere in reciprocal space. No temperature dependence can be observed, *i.e.* the discs reflect static disorder. The profiles appear to be independent of crystal location. Due to their small widths and because they

are centred at Bragg positions, disc intensities are heavily affected by tails of Bragg reflections, which makes even a qualitative interpretation difficult.

4.3.3. Sharp diffraction in Bragg layers from twinning and from an additional crystal phase. Five lattices based on two unit cells of different dimensions and different orientations are necessary to index all reflections in the Bragg layers. Two sets of weak but sharp reflections are related to the strong Bragg peaks through rotations of **a*** and **b*** around **c*** by $\pm 65.7^\circ$. The corresponding twin law is best described in terms of the primitive reciprocal basis $\mathbf{a}^*_{\rm prim} = (\mathbf{a}^* + \mathbf{b}^*)/2$ and $\mathbf{b}^*_{\rm prim} = (\mathbf{a}^* - \mathbf{b}^*)/2$: $\mathbf{a}^*_{\rm prim}$ of one small twin domain coincides with $\mathbf{b}^*_{\rm prim}$ of the large twin domain and *vice versa* for the second small domain (see Fig. 3*a*). Rotational twinning of the centred orthorhombic lattice is easily understood as a consequence of its pseudo-hexagonal metric with $|\mathbf{a}|_{\rm prim} = 13.98$ Å and $\gamma = 114.28^\circ$. Orthorhombic twin domains perfectly match at interfacing layers passing through centres of tunnels (Fig. 1) and spanned by $\mathbf{c}_h$ and $\mathbf{a}_{\rm prim}$ (or $\mathbf{b}_{\rm prim}$).

A further set of additional reflections is incompatible with the orthorhombic lattices, but can be indexed on the basis of a hexagonal or trigonal lattice with $|\mathbf{a}_{\rm hex}| = 14.32\ (1)$ Å (room temperature) and $\mathbf{c}_{\rm hex} = \mathbf{c}_h$. The direction of $\mathbf{a}^*_{\rm hex}$ coincides with $\mathbf{a}^*_{\rm prim}$ or $\mathbf{b}^*_{\rm prim}$ of the main twin domain, so that two orientations of hexagonal individuals can be observed. Apart from the 00*l* reflections the hexagonal lattice is completely incommensurate with the orthorhombic lattice. The volumes of hexagonal and (primitive) orthorhombic unit cells are about the same: 849 (1) and 852 (1) Å^3, respectively; the distribution of intensities is also very similar. This suggests a hexagonal or trigonal packing of PHTP molecules very similar to that of the orthorhombic structure with $\bar{6}$- or threefold axes parallel to the tunnels and passing through molecular centres. Assuming that the centre-to-centre distances between PHTP molecules in the hexagonal structure are comparable to those of the orthorhombic structure, $|\mathbf{a}_{\rm hex}|$ is expected to be 14.41 Å from the distance along **a** and 14.43 Å from the distance along **b**, close to the observed value $|\mathbf{a}_{\rm hex}| = 14.32\ (1)$ Å. No information about the guest structure of the hexagonal phase is available from the experimental data. It is not even clear whether the channels are filled or empty. The similarity in unit-cell volumes suggests that the hexagonal unit cells also contain guest molecules. In spite of all similarities with the orthorhombic structure, the presence of the hexagonal lattice is quite difficult to understand because orthorhombic and hexagonal lattices show no common periods in the **a*****b*** planes, *i.e.* no matching interfaces, and thus, domain walls between orthorhombic and hexagonal individuals must be highly disordered. As the volume fraction of the hexagonal domains is very low, it is not too surprising that no diffuse scattering from these domain walls can be seen.

Intensities from all small individuals decrease steeply with increasing $|l_h|$. Scattering from hexagonal or orthorhombic twins cannot be seen in the satellite layers. Reflections belonging to the hexagonal lattices are generally stronger than those from the weak orthorhombic twin domains. At the centre of the crystal twin reflections from the small orthorhombic domains do not change on going to low temperature, whereas they disappear at the free tip. The symmetry of twin reflections appears to be *mmm* for all data sets, except for the low-temperature data from the free tip, where the two hexagonal individuals are present in different portions, so that the symmetry of the *intensities* is reduced to monoclinic. At low temperature, reflections belonging to the hexagonal lattices smear out around **c*** by a few degrees and split in radial directions. This indicates a phase transition with a drastic increase in mosaicity. The transition is similar to that described for the cyclohexane inclusion compound (Mayo *et al.*, 1999).

4.4. Scattering in the satellite layers

4.4.1. Sharp satellite scattering. Satellite reflections are found in **a*****b*** layers at $|l_h| = 0.2$, 0.4, 0.6, 0.8, 1.2... (l_h is non-integer). All satellites appear to be completely sharp along **c***, but slightly broadened within the **a*****b*** planes. Up to two orders of satellites can be observed at the crystal centre and at the glued tip, up to three orders at the free tip. The strongest intensities are found in layers next to Bragg layers, *i.e.* for first-order satellites, and in areas where diffuse columns (11) pass through satellite layers (Figs. 5–7). On layers with $|l_h| = 0.4n$ (n an integer) strong satellite intensities cluster in broad bands extending along **b*** (Figs. 2*d*, 6 and 8). On layers with $|l_h| = 0.2(2n + 1)$, satellite intensities which are not on diffuse columns increase with increasing $|k|$, but are absent at $k = 0$ (Figs. 5 and 7). A comparison of these patterns with the form factors $\overline{f}_{\rm PHTP}$ and $f_{\rm NPP_2}$ shows the influence of both. It can be concluded that the satellites are due to mutual modulations of the two substructures. These modulations are not a direct consequence of *R*/*S* disorder because satellite intensities on the diffuse columns seem to be governed mainly by $\overline{f}_{\rm PHTP}$.

The *positions* of the satellites show orthorhombic *mmm* symmetry for all data sets. The *intensities* match this symmetry (Fig. 2*d* and 6*a*), except for the free tip of the crystal where it is clearly broken (Figs. 5, 6*b* and 7*b*). Satellite scattering of the crystal investigated by Weissenberg techniques is very similar, monoclinic at the tip mounted to the glass fibre, and orthorhombic at the centre and at the free tip of the crystal. Satellites are sharp, but are accompanied by underlying, very narrow, but clearly diffuse spots. The presence of two sets of unequal satellites indicates a twin structure in which the domains are related by the mirror plane 0*kl*. Note the difference to the twinning with respect to *h*0*l* described in §4.3.3. Here, the twinning is in the modulations of the major orthorhombic domain, *i.e.* in different parts of the same three-dimensional lattice. Owing to the monoclinic intensity distribution, the satellite reflections have been indexed in terms of twinned (3 + 1)-dimensional monoclinic lattices (**b** axis unique). These are systematical absences in the *h*0*l* layer at $|l_h| = 0.2$, 1.8, 2.2 and 3.8, suggesting the satellite vector $\mathbf{q} = 0.64\mathbf{a}^* + 0.8\mathbf{c}^*$ for all data sets (Fig. 4).

The ratio of modulation twins is approximately independent of temperature for all data sets except for the free tip at low temperature, where satellites become visible which are too weak to be seen in the corresponding room-temperature data

(Figs. 6–8). This means that at the free tip long-range order of mutual host–guest modulations becomes more pronounced at low temperature.

A more detailed analysis of the symmetry, metric aspects and intensities of satellite reflections will be given in a forthcoming paper, where results from refinement of satellite intensities will be presented.

König *et al.* (1997) attributed an additional system of satellites to positions $h + k$ = odd in second-order satellite layers with $|l_h|$ = 0.4, 0.6, 1.4, 1.6... . In our experiments only streak-like scattering parallel to **a*** (see below) can be observed at these positions. The putative satellites in the 0*kl* precession photographs of König *et al.* (1997) are probably cross sections through these streaks.

4.4.2. Diffuse scattering in satellite layers. Diffuse scattering around satellite layers is narrow, asymmetric, but not completely sharp along **c***. The most dominant diffuse features in layers with first-order satellites ($|l_h|$ = 0.2, 0.8, 1.2, 1.8...) are streaks along **a*** centred at positions $h + k =$ even (Figs. 5, and 6*a* and *b*), *i.e.* the streaks interconnect satellites from different twin domains across the larger of the two gaps. They are narrow, but not completely sharp perpendicular to the streak direction. At the intersection with columns (11) a few streaks interconnect satellites along directions which are pseudo-hexagonal equivalents of **a***. The symmetry of the diffuse features is *mmm* even at the free tip where the symmetry of sharp satellites is monoclinic. The appearance of the streak pattern is very similar at all crystal locations and at all temperatures.

Layers with second- and third-order satellites ($|l_h|$ = 0.4, 0.6, 1.4, 1.6, 2.4...) differ from those with first-order satellites, not only with respect to the intensity distribution, but also with respect to their dependence on crystal locations. At the crystal centre and at the glued tip, streak-like scattering interconnects positions of second-order satellites from the two twin domains. In contrast to first-order satellite layers, the streaks are centred mainly at $h + k =$ odd and always oriented parallel to **a***; they connect satellites from different twin domains across the shorter gap. They are narrow, but not completely sharp along **b*** and are connected by broad diffuse bands parallel to [11] and $[\bar{1}\ 1]$ (Fig. 7*a*). Generally, the streaks are most intense at positions of diffuse columns and at positions close to $h = 0$. No streaks can be observed at $k = 0$ and intensities increase with increasing $|k|$. An interesting observation is that some streaks are also interconnecting positions where sharp satellites are expected, although the latter are not observable. In layers *hk*1.6 and *hk*2.4 a second set of broad diffuse lines parallel to **b*** can be found at small h and k, where the molecular form factor f_{NPP_2} of the guest is large (Fig. 8*a*). These features are not seen in the region of the columns and may thus be assigned to the guest. Diffuse intensities in second-order satellite layers from the centre and from the glued tip follow approximate *mmm* symmetry and show no obvious dependence on temperature.

At the free tip, the general appearance of diffuse intensity is very similar to that at the crystal centre and the glued tip. The finer details are significantly different, however. The streak-like scattering observed at the crystal centre changes to broad features narrowing towards the satellites (Fig. 7*b*). In the layers *hk*1.6 and *hk*2.4 the diffuse intensities become triangular and connect three second-order satellite reflections (Fig. 8*b*). This reduces the symmetry of diffuse intensities in second-order satellite layers to monoclinic (**b** axis unique).

The satellite layers show complementary modulations in the regions of the diffuse columns similar to those described for the columns in the Bragg layers (§4.2.3). The broad local minima in *hk*0.2, *hk*0.4, *hk*1.6, *hk*1.8 *etc.* are accompanied by the corresponding maxima in layers *hk*0.6, *hk*0.8, *hk*1.2, *hk*1.4 *etc.* (*cf.* Fig. 5 with Fig. 2*d*, and 6*a* and *b*). These observations apply to all crystal locations at both temperatures. However, the pattern is not as clear as in the Bragg layers because diffuse intensities in the satellite layers are much weaker and partly superimposed by diffuse tails from Bragg layers. Within all layers a variety of very broad irregular modulations of weak background intensities can be observed.

The diffuse scattering in all satellite layers reflects the influence of both $\overline{f}_{\mathrm{PHTP}}$ and f_{NPP_2}, as does the satellite scattering. It can therefore be assigned to a disorder associated with the modulation wave and affecting both host and guest molecules. Streak-like diffuse scattering which interconnects sharp diffraction spots is often due to domain walls (Boysen, 1995). This interpretation fits the observations from $PHTP_5$·NPP quite well, as the streaks always interconnect satellites belonging to different twin domains. In the absence of a valid interpretation of the satellites, and thus of the mutual interactions between host and guest molecules, a more detailed interpretation of diffuse scattering in satellite layers cannot yet be given.

5. Summary

The $PHTP_5$·NPP inclusion compound exhibits unusually complex scattering of different dimensionality. Apart from sharp (zero-dimensional) Bragg and satellite reflections, a number of (nearly) one-dimensional, (nearly) two-dimensional and three-dimensional diffuse scattering phenomena can be observed. Some of the features are remarkable because their shape and symmetry depend on the location in the crystal, implying that the crystal is not homogeneous along the needle axis. Most of the diffraction phenomena could be assigned to occupational disorder of *R*- and *S*-PHTP, to displacive disorder of the host substructure, to positional disorder of the guest substructure, and to mutual modulation of the two substructures or to combinations of these. Assignment is greatly facilitated by (i) comparisons of the experimental data with the relevant combinations of form factors of host and guest molecules that are nicely separated in reciprocal space, and (ii) the different temperature dependence of the various diffraction phenomena.

In this work we have shown that the combination of synchrotron radiation, a high-performance area detector and powerful software allow easy recording and reduction of complete, three-dimensional diffuse data of high quality in a reasonably short time. It is thus now feasible to obtain

complete information on diffuse intensities from disordered crystals under different conditions and for slightly different chemical compositions. Such data can be extremely helpful in finding trial models of structural disorder, *i.e.* in solving the 'phase problem' of disordered crystals (for examples see Frey, 1995, 1997; Welberry & Butler, 1995). Qualitative interpretations, such as are described here, constitute only the first of three steps aimed at a determination of real (as opposed to ideal) crystal structures. In the second step the qualitative interpretations are translated into a quantitative model of disorder and reasonable initial estimates of its numerical parameters are determined. In the third step the final model is refined to best fit the experimental data.

The analysis of complex diffuse data is still far from being routine. Recently developed automatic Monte Carlo methods (Welberry *et al.*, 1998) constitute a powerful tool for *refining* models of relatively complicated disordered systems (*e.g.* Welberry, 2000). The use of automated Monte Carlo methods for *finding* such models would require computational power that is not available at present. We have therefore attempted to derive such information from a comparative interpretation of the disordered average structure and the diffuse diffraction pattern. Although the visual interpretations described in this work may be educational, automated procedures for 'reading' reciprocal space would be preferable; however, at present such procedures remain a challenge for the future.

We thank the staff of the Swiss–Norwegian Beamline at ESRF, especially Philip Pattison, and Henrik Birkedal, Institute of Crystallography, University of Lausanne, for their help during the preparation and realisation of the experiment. We also thank Professor Jürg Hulliger, Department of Chemistry and Biochemistry, University of Berne, for samples of the material. This work was supported by the Swiss National Science Foundation.

References

Allegra, G., Farina, A., Immirzi, A., Colombo, A., Rossi, U., Broggi, R. & Natta, G. (1965). *J. Chem. Soc. B*, pp. 1020–1028.
Boysen, H. (1995). *Phase Transit.* **55**, 1–16.
Cahn, R. S., Ingold, C. K. & Prelog, V. (1966). *Angew. Chem. Int. Ed. Engl.* **5**, 385–415.
Estermann, M. A. & Steurer, W. (1998). *Phase Transit.* **67**, 165–195.
Farina, M. (1984). *Inclusion Compounds 2*, edited by J. L. Atwood, J. E. D. Davis & D. D. MacNicol, pp. 69–95. London: Academic Press.
Farina, M., Di Silvestro, G. & Sozzani, P. (1997). *Comprehensive Supramolecular Chemistry*, Vol. 6, *Solid-State Supramolecular Chemistry: Crystal Engineering*, edited by D. D. MacNicol, F. Toda & R. Bishop, pp. 371–398. Oxford: Elsevier Science.
Frey, F. (1995). *Acta Cryst.* B**51**, 592–603.
Frey, F. (1997). *Z. Kristallogr.* **212**, 257–282.
Hoss, R., König, O., Kramer-Hoss, V., Berger, U., Rogin, P. & Hulliger, J. (1996). *Angew. Chem. Int. Ed. Engl.* **35**, 1664–1666.
Hulliger, J., König, O. & Hoss, R. (1995). *Adv. Mater.* **7**, 719–721.
Hulliger, J., Roth, S. W., Quintel, A. & Bebie, H. (2000). *J. Solid State Chem.* **152**, 49–56.
Kabsch, W. (1988*a*). *J. Appl. Cryst.* **21**, 67–71.
Kabsch, W. (1988*b*). *J. Appl. Cryst.* **21**, 916–924.
Kabsch, W. (1993). *J. Appl. Cryst.* **26**, 795–800.
König, O., Bürgi, H. B., Armbruster, Th., Hulliger, J. & Weber, Th. (1997). *J. Am. Chem. Soc.* **119**, 10632–10640.
Mayo, S. C., Proffen, Th., Bown, M. & Welberry, T. R. (1999). *J. Appl. Cryst.* **32**, 464–471.
Prelog, V. & Helmchen, G. (1982). *Angew. Chem. Int. Ed. Engl.* **21**, 567–583.
Scheidegger, S., Estermann, M. & Steurer, W. (2000). *J. Appl. Cryst.* **33**, 35–48.
Welberry, T. R. (2000). *Acta Cryst.* A**56**, 348–358.
Welberry, T. R. & Butler, B. D. (1994). *J. Appl. Cryst.* **27**, 205–231.
Welberry, T. R. & Butler, B. D. (1995). *Chem. Rev.* **95**, 2369–2403.
Welberry, T. R., Proffen, Th. & Bown, M. (1998). *Acta Cryst.* A**54**, 661–674.